

# Efficient X-ray generation from gold colloidal solutions

Koji Hatanaka<sup>1,\*</sup>, Matteo Porta<sup>2</sup>, Frances Camille P. Masim<sup>1</sup>, Wei-Hung Hsu<sup>1</sup>, Mai Thanh Nguyen<sup>2</sup>, Tetsu Yonezawa<sup>2</sup>, Armandas Balčytis<sup>3,4</sup>, and Saulius Juodkazis<sup>3,5</sup>

<sup>1</sup>Research Center for Applied Sciences, Academia Sinica, Nangang, Taipei 11529, Taiwan

<sup>2</sup>Department of Materials Science, Graduate School of Engineering, Hokkaido University, Sapporo 060-8628, Japan

<sup>3</sup>Faculty of Science, Engineering and Technology, Swinburne University of Technology, Hawthorn, VIC 3122, Australia

<sup>4</sup>Institute of Physics, Center for Physical Sciences and Technology, Vilnius, LT-02300, Lithuania

<sup>5</sup>Center for Nanotechnology, King Abdulaziz University, Jeddah 21589, Saudi Arabia

\*kojihntk@gate.sinica.edu.tw

## ABSTRACT

Hard X-ray generation for Au nanoparticle dispersion was systematically investigated for different particle diameters ranging from 10 to 100 nm with a narrow size distribution of  $\pm 2\%$ . Scaling law of X-ray generation is close to a 6-photon process before the onset of saturation for excitation by 45 fs laser pulses with central wavelength of 800 nm. This is consistent with bulk plasmon excitation at  $\lambda_p^{bulk} \simeq 138$  nm. The longitudinal E-field component due to nanoparticle focusing is responsible for the excitation of the longitudinal bulk plasmon. The proposed analysis also explains X-ray emission from water breakdown via an electron solvation mechanism at  $\sim 6.2$  eV. The most efficient emission of X-rays was observed for  $40 \pm 10$  nm diameter nanoparticles which also had the strongest UV extinction. X-ray emission was the most efficient when induced by pre-chirped  $370 \pm 20$  fs laser pulses and exhibited the highest intensity at a negative chirp.

## Introduction

Compact and efficient hard X-ray sources can revolutionize biological and medical fields as well as practical applications. Liquid targets for X-ray generation by optically induced breakdown are attractive due to the possibility to tailor the X-ray spectrum via choice of ion content of the micro-jet or droplet irradiated by high intensity laser pulses at  $\sim 10^{15}$  W/cm<sup>2</sup>.<sup>1</sup> At even higher intensities approaching  $\sim 10^{20}$  W/cm<sup>2</sup> (in vacuum), particle acceleration beams for electrons and protons up to MeV energies are demonstrated using peta-watt lasers.<sup>2</sup>

In the case of ultra-short laser pulses, a wide range of control parameters over light-matter interaction exist, some of which, are specific to the ultrashort laser pulses: spatial and temporal chirp. Polarisation, optical nonlinearities of irradiated materials, different contributions of E-field components due to peculiarities of focusing at the near-field, provide ways to enhance electron temperature and concentration for brighter X-ray emission as briefly introduced below.

It has been demonstrated that the resonant absorption mechanism is responsible for hard X-ray generation in the case of metal-doped glasses<sup>3</sup> and water jets<sup>4,5</sup> irradiated by  $\sim 150$  fs pulses. By introduction of a negative chirp and choosing p-polarized pulses, X-ray generation is enhanced by almost an order of magnitude.<sup>5</sup> For 5-6 times shorter pulses, the multi-photon ionization (MPI) becomes comparable to or more efficient than impact ionization (IMP), and even higher electron densities and temperatures are reached.<sup>6-8</sup> In the case of X-ray generation from wide-bandgap undoped dielectrics such as pure silica, sapphire, or water with high dielectric strength against dielectric breakdown, the polarization dependent rates of MPI become important, especially for short sub-50 fs pulses. Surface breakdown intensity of silica and sapphire scales as  $I^{cir}/I^{lin} \propto 1/\sqrt{N} \sqrt{\sigma_N^{cir}/\sigma_N^{lin}}$ , where  $\sigma_N$  is the corresponding  $N$ -photon absorption cross section defining the rate of the ionization.<sup>9</sup> The linear polarization is more efficient in ionization as compared with circular, this trend is observed up to an irradiance of  $\sim 30$  TW/cm<sup>2</sup>.<sup>9</sup>

However, once the plasma is formed, the electron quiver energy is likewise polarization dependent and becomes twice larger for the *circular* polarization as compared with *linear* according to  $\epsilon_{osc} \propto (1 + \alpha^2)$ , where  $\alpha = 0, 1$  for linear and circular polarization, respectively.<sup>6,7</sup> The IMP and MPI rates are dependent on the  $\epsilon_{osc}$  as  $w_{mpi} \propto \epsilon_{osc}^N$  and  $w_{imp} \propto \epsilon_{osc}$ ; hence, more efficient ionization is expected for circularly polarized pulses.<sup>6</sup>

The chirp effect at high irradiance is also expected to influence the ionization rates, especially when photon energy is close

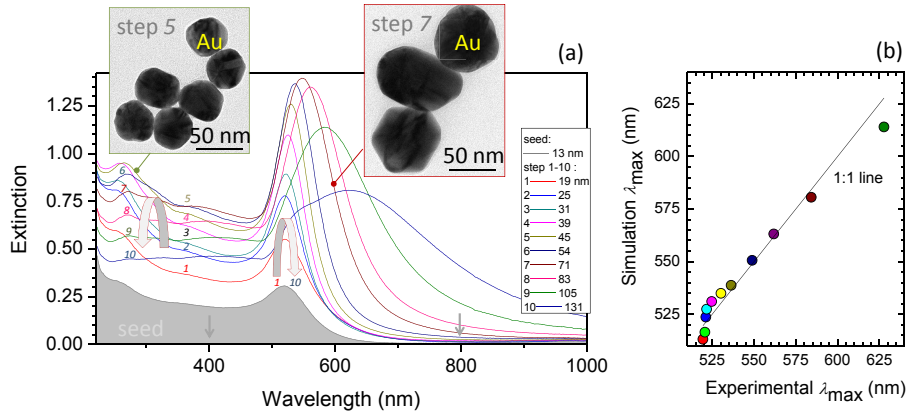


**Figure 1.** (a) Experimental extinction spectra of Au nanoparticle dispersion at different growth stages (steps from 1 to 10); a 1:3 (sample:water) dilution was used in all spectroscopically investigated samples as compared to the solution used for X-ray generation. Insets show TEM images of 45 and 71-nm-diameter nanoparticles (steps 5 and 7, respectively). The central wavelength of the fundamental (800 nm) and second harmonics (400 nm) of the fs-laser excitation are marked. The average diameters of Au nanoparticles were extracted from TEM images for the different steps of growth. (b) Numerically simulated extinction spectra of spherical Au nanoparticles; the diameters were determined experimentally by TEM imaging (see, (a)). Simulations were carried out using Lumerical FDTD Solutions software.

to the fundamental absorption of a target material. By introducing a negative chirp with shorter wavelength (a larger photon energy) at the leading part of the pulse, ionization rates can be significantly enhanced due to  $\epsilon_{osc}^N$  dependence of  $w_{mpi}$ . Then, the trailing red-shifted (in wavelength) part of the pulse will contribute more efficiently to the ionization and heating of plasma due to the  $w_{imp} \propto \lambda^2$  scaling.<sup>5,6</sup>

Creation of practical X-ray emitting sources depends on understanding the effects of temporal and spatial chirp,<sup>10</sup> polarization, as well as nonlinear phenomena in delivery of ultra-short laser pulses for X-ray generation at high irradiance conditions, especially when more complex targets such as colloidal dispersions and layered materials are used.

Here, it is shown that the most efficient X-ray emission was observed for Au nanoparticles of  $r \simeq 20$  nm radius under irradiation of negatively pre-chirped pulses which were approximately 8 times longer compared with the shortest 45 fs pulses. Chirp can be efficiently used to augment the X-ray emission by a factor of two over the intensity values observed using bandwidth limited excitation pulse duration. Power scaling of X-ray emission implies bulk plasmon generation in gold nanoparticles and absorption being the driving mechanism of X-ray emission. Numerical modelling of optical extinction of nanoparticles separated scattering and absorption contributions and confirmed the presence of a strong E-field component perpendicular to the surface, which is required to excite longitudinal bulk plasmons.

## Results

For the study of X-ray emission and for establishing its power scaling dependence it was essential to have a very narrow gold nanoparticle size distribution. For this study we used mono-dispersed solutions with  $< 2\%$  diameter distribution for the smallest colloidal nanoparticles up to 70 nm in size and  $< 6\%$  for the larger ones.

The extinction spectra of dispersions of various size Au nanoparticles is shown in Fig. 1 (a). Strong losses at the UV spectral range do not have a resonant character and are dominated by the *d*-to-*sp* Au interband transitions. On the other hand, the plasmonic resonance region around 520 - 600 nm depends on the nanoparticle size.<sup>11</sup> The strongest relative contribution at the UV wavelengths of 200-300 nm was observed for the 40-50 nm diameter nanoparticles which proved to facilitate the most efficient generation of X-rays. The resonant peak positions in extinction spectra were calculated using experimentally determined nanoparticle sizes for the step 1-10 generations of the colloidal dispersions. Figure 1(b) shows correlation between the experimental and numerical peak positions of the plasmonic resonance. In each case modeling was carried out for a single isolated spherical nanoparticle. Good correspondence between numerical and experimental results indicates that nanoparticle solutions had no agglomerated clusters nor had significant neighboring nanoparticle interaction effects. This also corroborates that dispersions were mono-dispersed in terms of nanoparticle size.

Figure 2 shows the power scaling of X-ray generation from 30-nm-diameter Au nanoparticle dispersion as well as  $\text{HAu}^{3+}\text{Cl}_4$  solution and water for reference. Strong increase of X-ray intensity is observed for lower pulse energies below 0.1 mJ, with subsequent saturation. The six photon processes can explain the initial steep power scaling which would

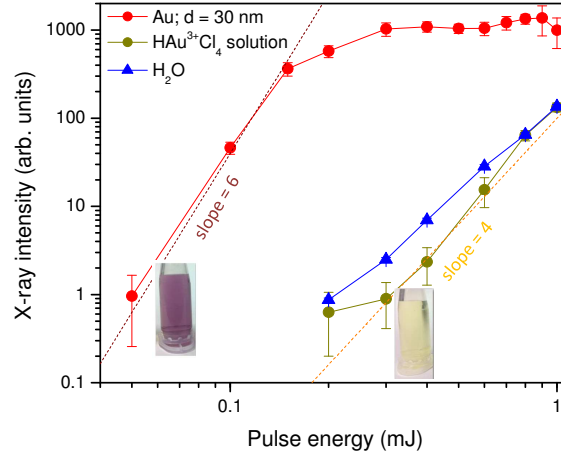


**Figure 2.** Intensity of X-ray emission vs pulse energy for  $r = 30$  nm radius Au nanoparticle aqueous dispersion,  $\text{HAu}^{3+}\text{Cl}_4$  solution and distilled water (data from different experiments). Laser pulses of  $t_p = 40$  fs duration and  $\lambda = 800$  nm central wavelength were focused with an objective lens of  $NA = 0.2$  numerical aperture; insets show images of the solutions.

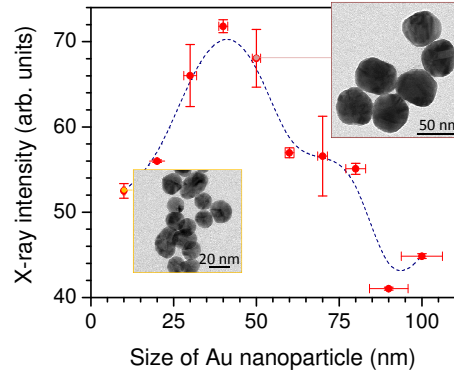


**Figure 3.** X-ray intensity vs Au nanoparticle diameter ( $2r$ ). Au concentration was 1.2 mmol in all samples. Horizontal error bars represent the standard deviation of particle diameter and vertical error bars represent the X-ray intensity measurements performed three times between 30 min intervals. Pulse energy was  $E_p = 0.5$  mJ.

correspond to a 133 nm wavelength. For the electron density in gold  $N_e = 5.90 \times 10^{22} \text{ cm}^{-3}$  the bulk plasmon frequency of  $\omega_p = \sqrt{\frac{N_e e^2}{m_e m^* \epsilon_0}}$  corresponds to the wavelength  $\lambda_p^{\text{bulk}} = 138$  nm, considering that the effective electron mass is  $m^* = 1$ ,  $m_e$  and  $e$  are the free electron mass and charge, respectively. Usually, the effective electron mass in metals is 20-30% lower due to periodicity of the lattice. The 6-photon process, indeed, is probable for excitation of the bulk plasmon, which is a longitudinal wave and cannot be directly excited by transverse E-field of the incident light. However, the bulk plasmon can be excited by the longitudinal component of the light field which is comparable with the total field for the 30-50 nm diameter particles.<sup>12</sup>

The power scaling of X-ray generation in water and  $\text{HAu}^{3+}\text{Cl}_4$  solution (Fig. 2) exhibits a slope consistent with a 4-photon process. Interestingly, the 4-photon absorption would correspond to the  $\sim 6.2$  eV energy which was for a long time assumed as the band gap energy of water and would be in accordance with water breakdown. However, recently it was demonstrated that this energy corresponds to the creation of a solvated electron complex out of the valence band in pure water<sup>13</sup> while the bandgap of the water is  $\sim 9.5$  eV. The slope of the 4-photon process in water and  $\text{HAu}^{3+}\text{Cl}_4$  solution is consistent with breakdown ionisation of water at the irradiation conditions used.

A systematic study of X-ray emission dependence on particle size is shown in Fig. 3. For the diameters  $2r = 40$  nm the strongest X-ray emission was observed in the saturated region of the power dependence (Fig. 2). Intensity of X-ray emission measured in air is strongly absorbed at the low energy soft X-ray spectral region (Fig. 4(a)). However, when presence of hard X-rays with photon energy  $E > 7$  eV is substantial, the black body emission fitting allows to extract the electron temperature

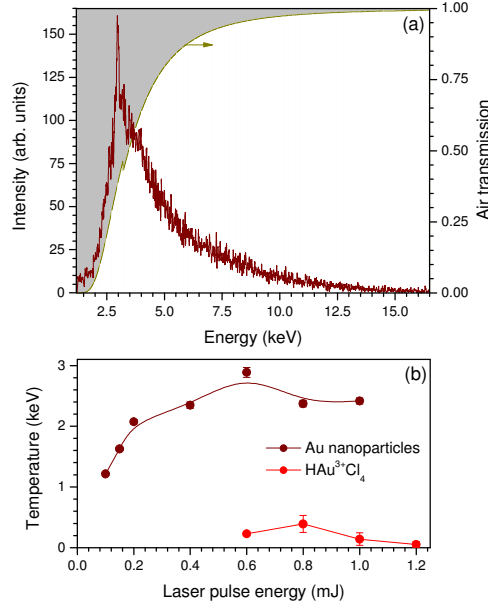


**Figure 4.** (a) X-ray emission spectrum and air transmission. (b) Temperature of electrons,  $T_e$ , deduced from the black body fit of emission from dispersion of Au colloidal particles  $2r = (30 - 40)$  nm and 2.5 mM solution of  $\text{HAu}^{3+}\text{Cl}_4$ .

$T_e$  from the Planck's formula:

$$I(\nu, T) = \varepsilon \frac{2h\nu^3}{c^2} \frac{1}{\exp(h\nu/kT) - 1}, \quad (1)$$

where  $T$  is the absolute temperature of the emitter,  $h$  is the Planck constant,  $\nu = c/\lambda$  is the frequency of the electromagnetic radiation,  $c$  is speed of light in vacuum,  $\lambda$  is the wavelength, and an emissivity  $\varepsilon \equiv 1$  is assumed for the black body conditions. The results of the fitting using Eqn. 1 are shown in Fig. 4(b). Electron temperatures  $T_e \simeq 2.5$  keV are reached for the Au nanoparticle dispersion at the most efficient X-ray emission conditions. An order of magnitude lower emission of X-rays were observed in a 2.5 mM concentration aqueous solution of  $\text{HAu}^{3+}\text{Cl}_4$ .

Influence of the temporal chirp on X-ray emission is presented in Fig. 5. When  $\Phi_2 \simeq \pm 6000$  fs<sup>2</sup> the strongest emission was observed as compared with bandwidth limited pulse duration of  $t_0 = 45$  fs. The  $\Phi = 6000$  fs<sup>2</sup> correspond to a pulse duration  $t_p \simeq 372$  fs. Negative chirp is slightly more efficient in X-ray generation as was earlier observed in jets.<sup>5</sup>

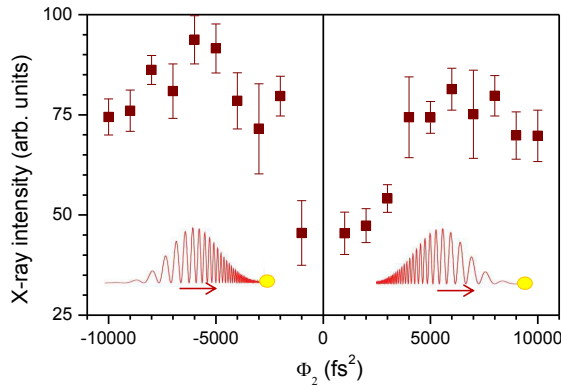


**Figure 5.** Chirp effect: X-ray intensity vs. the second order dispersion  $\Phi_2$  [fs<sup>2</sup>];  $\Phi_1 \equiv 0$ . Insets depict chirped pulse irradiating a gold nanoparticle. Pulse duration resulting in the strongest X-ray emission at  $\Phi_2 = \pm 6000$  fs<sup>2</sup> is  $t_p = 372$  fs while the shortest pulse was  $t_p = 45$  fs at  $\Phi_2 = 0$ .

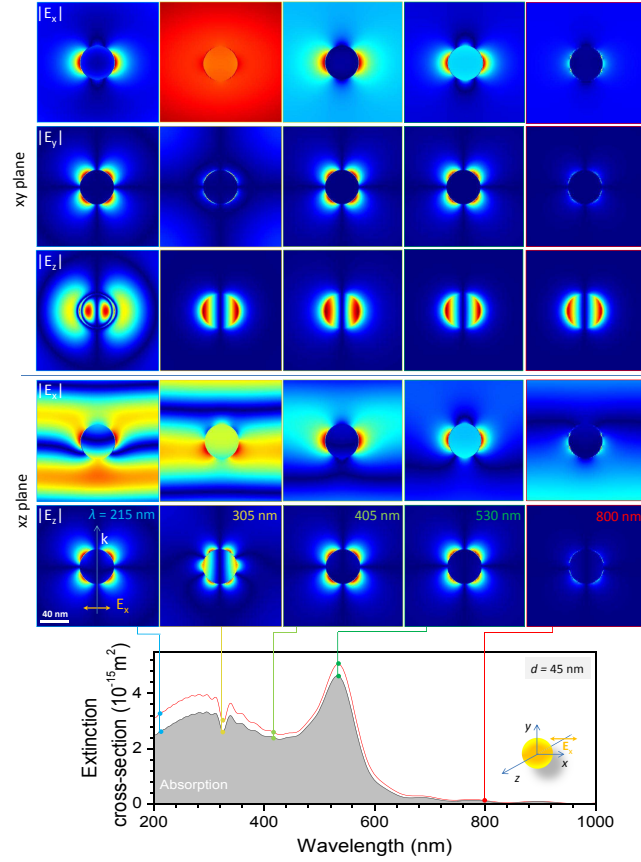


**Figure 6.** The calculated absorption and total extinction spectra for a 45 nm diameter Au nano-sphere in water. Schematic E-field distributions for the different components illustrate the features of light localisation at several characteristic spectral locations. The longitudinal  $E_z$  field component in xz- and xy-planes are important for excitation of bulk plasmons; the incident field is  $E_x = 1$ ,  $\mathbf{k}$  is the propagation direction of light.

## Discussion

Frequencies of the surface plasmon polariton and the bulk plasmon are related as  $\omega_{SP} = \omega_b/\sqrt{2}$ . For the  $\lambda = 0.8 \mu\text{m}$  wavelength ( $\omega = 2\pi c/\lambda$ ) radiation used the 6-photon process, which matches the bulk plasmon energy in gold, corresponds to  $\hbar\omega_b = 9.2 \text{ eV}$ , whereas surface plasmon polariton energy is  $\hbar\omega_{SP} = 6.5 \text{ eV}$ . These plasmon excitations are defined by the electronic properties of gold and are independent from the particle size and shape which define the resonances at visible wavelengths (see, Fig. 1). The energy values of 9.2 and 6.5 eV match the plasma waves in gold and the energy required to create a solvated electron in water, respectively.<sup>13</sup> The observed power law of X-ray emission suggests that the light energy absorption pathway is via the bulk plasmon excitation for gold colloidal nanoparticles and the breakdown of pure water or solution (Fig. 2).

Earlier studies of Au colloidal particles in water under exposure by 400 nm/150 fs laser pulses showed that nanoparticles with radii  $r = (20 - 25) \text{ nm}$  require the smallest fluence to be disintegrated. At this size nanoparticles absorb enough energy for disintegration (explosion) whereas for the smaller nanoparticles melting occurs. It is noteworthy, that such size does not correspond to the resonant plasmon band (see, Fig. 1). It was shown recently that explosion of a gold nanoparticle proceeds via electron ejection from its surface.<sup>14</sup> This is very similar to the formation of a solvated electron in water at the initial stage of water breakdown. For the electron ejection, an E-field component perpendicular to the surface of a Au nanoparticle is essential. Earlier demonstration of the X-ray generation via resonant absorption of the longitudinal E-field component,<sup>5</sup> photocatalysis<sup>12,15,16</sup> and ablation<sup>17</sup> perpendicular to the surface are consistent with the proposed conjecture that the longitudinal field component plays a key role in absorption and electron heating resulting in the X-ray generation from the Au colloidal particle solution. Even though a strong incident  $E_x$  component is perpendicular to the surface at the equator of a nano-sphere, it creates a strong reflection and energy is not absorbed, while the longitudinal component  $E_z$  is absorbed<sup>18</sup> (hence, the resonant absorption).

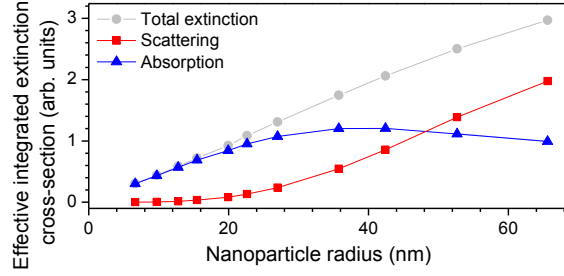


**Figure 7.** The FDTD simulated extinction, absorption, and scattering cross sections of different size spherical Au nanoparticles, integrated over the  $200 \text{ nm} \leq \lambda \leq 1000 \text{ nm}$  spectral span shown in Fig. 6 and normalized to the corresponding geometrical cross-sections;  $\sigma_{ex} = \sigma_{sc} + \sigma_{ab}$  [ $\text{cm}^2$ ].

To reveal the absorption contribution in the total extinction due to a gold nanosphere in water the cross sections were calculated, where  $\sigma_{ex} = \sigma_{sc} + \sigma_{ab}$  (Fig. 6). Furthermore, spatial distributions of E-field components around particle were extracted. For the linearly polarised  $E_x \equiv 1$  beam incident on the nano-sphere with the optimum size  $2r = 45 \text{ nm}$  for X-ray generation (see, Fig. 3), the total extinction has a contribution of absorption that is significantly larger than scattering (Fig. 7). The spectrum and volume integrated cross sections, normalized to the geometrical cross-sections of the Au particles are shown in Fig. 7. The largest values of an integral absorption over the range of visible wavelengths mark the size region of nanoparticles for the most efficient X-ray generation.

The insets in Fig. 6 show maps of the E-field components, including the longitudinal field  $E_z$  in the  $xz$ - and  $xy$ -planes, for the beam propagating along  $z$ -axis ( $\mathbf{k} \parallel \mathbf{z}$ ). The light penetration depth into the particle is limited to the skin depth, however, there are peculiar spectral positions for the  $E_z$  component for a particular particle size (see  $\lambda = 305 \text{ nm}$  in Fig. 6) where absorption is slightly smaller yet light field penetration is substantial. Hence, such anti-resonances in extinction and  $E_z$  longitudinal component contribute to the absorption and energy delivery from the light pulse to a nanoparticle via resonant absorption (an oscillating dipole aligned with the linear polarisation of the exciting beam would increase reflection and reduce absorption<sup>18</sup>). Due to its longitudinal character, this  $E_z$  field can excite a bulk plasmon. The  $E_z$  component in the  $xy$ -plane reveals its strong presence inside the nanoparticle which is expected to cause substantial absorption.

Generation of hard X-rays from a 2.5 keV temperature plasma described here is an efficient process in this part of EM spectrum. Conversely, for 1 THz ( $300 \mu\text{m}$ ) radiation the Eqn. 1 predicts a  $4.6 \times 10^{11}$  times smaller radiance as calculated for the black body heated to 5 keV (with peak emission at  $2.46 \text{ \AA}$ ). The emitted photon number ratio, between X-rays and T-rays at correspondingly  $2.46 \text{ \AA}$  and  $300 \mu\text{m}$  wavelength is, however, significantly smaller  $3.8 \times 10^5$ . Hence, terahertz emission from breakdown plasmas can be intense enough for use in applications,<sup>19,20</sup> however, in the case of water solutions a back-scattering geometry has to be used for the T-ray source due to strong water absorption.

## Conclusions

Hard X-ray emission from aqueous solution jets of 30-50 nm diameter Au nanoparticles is demonstrated to follow a 6-photon process consistent with bulk plasmon excitation in gold. Formation of the longitudinal component of the incident light field  $E_z$  ( $z$  is the propagation direction  $\mathbf{k} = 2\pi/\lambda$ ) required for excitation of bulk plasmon is due to near-field focusing by gold colloidal nanoparticles. Electron temperatures corresponding to the black body radiation of 2.5 keV produce a bright hard X-ray source which can be used in air conditions. Temporal chirp of 45 fs pulses provides a tool to control X-ray intensity. This mechanism is additionally corroborated by the X-ray generation scaling power law for water and is consistent with electron ejection from water molecule and formation of solvated electron at  $\sim 6.5 \text{ eV}$ .<sup>13</sup>

Creation of high temperature plasma fragmentation of colloidal particles in solution opens rich possibilities to investigate temporal dynamics of the breakdown on sub-wavelength scales and at short time windows where modeling is already predicting different scenarios to be cross checked and validated experimentally.<sup>13,14</sup> Laser-driven explosions with high temperature black body radiation can provide not only hard X-ray sources but also efficient THz emitters. Further studies are strongly required for directionality control for such EM-radiation to be used in practical applications.

## Methods

Ultra-short laser pulses were used for X-ray generation: pulse duration was  $t_0 = 45 \text{ fs}$  at the central wavelength of  $\lambda = 800 \text{ nm}$ , pulse energy typically ranged from  $E_p = 0.1 \text{ mJ}$  to  $1 \text{ mJ}$ , at  $1 \text{ kHz}$  repetition rate. Focusing was carried out with an off-axis parabolic mirror with focal length  $f = 5 \text{ cm}$  in air at atmospheric pressure; the equivalent numerical aperture of focusing was



$NA = 0.2$ . Pulse can be described by a Gaussian temporal envelope of the form  $E(t) = E_0 e^{-2\ln 2(t/t_p)^2} \cos(\omega t + \beta t^2)$ , where  $\omega$  is the cyclic frequency of light,  $t_p$  is the pulse duration at the full-width at half maximum (FWHM),  $\beta$  [1/fs<sup>2</sup>] is the linear chirp, and  $E_0 = \sqrt{2I_0/(c\epsilon_0 n)}$  is the field amplitude,  $n$  is the refractive index,  $c$  is speed of light,  $t$  is time,  $I_0 = 2I_{av}$  is the peak intensity which is twice larger than the average,  $I_{av}$  for the Gaussian, and  $\epsilon_0$  is the permittivity of vacuum. The instantaneous cyclic frequency  $\omega_{ins}(t) = \omega_0 + 2\beta t$ , where  $\beta > 0$  corresponds to the positive chirp with trailing high frequency components.

Pulse pre-chirping is implemented to increase pulse duration up to ten times using a 1D array of liquid crystal cells (FemtoJock, Biophotonics Solutions, Inc.). For the slowly with frequency  $\omega$  varying spectral phase  $\varphi(\omega)$  it can be expanded into the Taylor series around the central frequency  $\omega_0$  with the few first terms as  $\varphi(\omega) = \varphi(\omega_0) + \Phi_1 \omega + \frac{\Phi_2}{2!} \omega^2 + \dots$ , where  $\varphi(\omega_0)$  is the absolute phase of the pulse in time domain, the first derivative  $\varphi'(\omega_0) = \Phi_1$  is the group delay (GD) which defines a shift of envelope in time domain,  $\varphi''(\omega_0) = \Phi_2$  [fs<sup>2</sup>] is the group delay dispersion (GDD) or the second order dispersion which defines the chirp in time domain. Duration of the time broadened pulse at FWHM is defined as  $t_p = t_0 \sqrt{1 + [4\ln 2 \Phi_2 / t_0^2]^2} \equiv t_0 \sqrt{1 + \beta^2}$  where  $t_0 = 45$  fs is the shortest spectral bandwidth limited pulse duration. For this study higher orders as well as  $\Phi_1$  were set to zero.

The pulse energy of  $E_p = 0.1$  mJ corresponds to the field strength  $E_0 = 4.23 \times 10^{11}$  V/m, which is much higher than the breakdown of dry air at  $6 \times 10^6$  V/m. This complicates the determination of the actual fluence and irradiance on the nanoparticle due to breakdown of air and water jet with colloidal particles as discussed in detail in the Sec. [Discussion](#). The power scaling of X-ray emission is used instead to reveal the mechanism of X-ray generation rather the incident fluence/irradiance onto a nanoparticle.

Gold nanoparticle colloidal aqueous dispersions with the Au atomic concentrations at  $1.2 \times 10^{-3}$  mol/L with different particle diameters ranging from 10 to 100 nm were used for X-ray generation. Nanoparticles were negatively charged and surfactant coated to prevent agglomeration. Figure 1 shows optical extinction, cumulative scattering and absorption losses, spectra measured in transmission. A water jet 1 mm in diameter was formed at the flow rate of 2.5 m/s and a laser beam was delivered onto to the front surface of the jet. Optimisation of the focal region placement was carried out for the highest yield of X-ray emission.

X-ray emission intensity measurements were carried out using a Geiger counter (model5000, Health Physics Instrument, Inc.). X-ray emission spectroscopy was performed using a solid-state detector (XR-100CR, PX2CR, Amptek).

Numerical modeling of extinction spectra and light field enhancement were carried out using finite difference time domain (FDTD) software package (FDTD Solutions, Lumerical Solutions Inc.). A uniform 0.5 nm 3D mesh was used, permittivity of gold was tabulated in software according to results reported by Johnson and Christy.<sup>21</sup>

## References

1. K.Hatanaka, Miura, T., Ono, H. & Fukumura, H. Photon energy conversion of IR femtosecond laser pulses into X-ray pulses using electrolyte aqueous solutions in air. In Nakajima, K. & Deguchi, M. (eds.) *Science of Superstrong Field Interactions*, 260 – 267. AIP Conf. Proc. (vol.634, 2002).
2. Murakami, M. & Tanaka, M. Generation of high-quality mega-electronvolt proton beams with intense laser driven nanotube accelerator. *Appl. Phys. Lett.* **102**, 163101 (2013).
3. Hatanaka, K. *et al.* Hard X-ray generation using femtosecond irradiation of PbO glass. *J. Non-Crystall. Solids* **354**, 5485 – 5490 (2008).
4. Hatanaka, K., Ono, H. & Fukumura, H. X-ray pulse emission from cesium chloride aqueous solutions when irradiated by double-pulsed femtosecond laser pulses. *Appl. Phys. Lett.* **93**, 064103 (2008).
5. Hatanaka, K. *et al.* Chirp effect in hard X-ray generation from liquid target when irradiated by femtosecond pulses. *Opt. Express* **16**, 12650–12657 (2008).
6. Gamaly, E. G. The physics of ultra-short laser interaction with solids at non-relativistic intensities. *Phys. Reports* **508**, 91 – 243 (2011).
7. Gamaly, E. G. & Rode, A. V. Physics of ultra-short laser interaction with matter: From phonon excitation to ultimate transformations. *Progr. Quant. Electron.* **37**, 215–323 (2013).
8. Malinauskas, M., Žukauskas, A., Bičkauskaitė, G., Gadonas, R. & Juodkazis, S. Mechanisms of three-dimensional structuring of photo-polymers by tightly focussed femtosecond laser pulses. *Opt. Express* **18**, 10209–10221 (2010).
9. Temnov, V. V., Sokolowski-Tinten, K., Zhou, P., El-Khamhawy, A. & von der Linde, D. Multiphoton ionization in dielectrics: Comparison of circular and linear polarization. *Phys. Rev. Lett.* **97**, 237403 (2006).
10. Akturk, S., Gu, X., Zeek, E. & Trebino, R. Pulse-front tilt caused by spatial and temporal chirp. *Optics Express* **12**, 4399 – 4410 (2004).

11. Link, S. & El-Sayed, M. A. Spectral properties and relaxation dynamics at surface plasmon electronic oscillation in gold and silver nanodots and nanorods. *J. Phys. Chem. B* **13**, 8410 – 8426 (1999).
12. Mizeikis, V., Kowalska, E. & Juodkazis, S. Resonant localization, enhancement, and polarization of optical fields in nano-scale interface regions for photo-catalytic applications. *J. Nanosci. Nanotechnol.* **11**, 2814–2822 (2011).
13. Linz, N. *et al.* Wavelength dependence of nanosecond infrared laser-induced breakdown in water: Evidence for multiphoton initiation via an intermediate state. *Phys. Rev. B* **91**, 134114 (2015).
14. Delfour, L. & Itina, T. E. Mechanisms of ultrashort laser-induced fragmentation of metal nanoparticles in liquids: Numerical insights. *J. Phys. Chem. C* **119**, 13893 – 13900 (2015).
15. Mizeikis, V., Kowalska, E., Ohtani, B. & Juodkazis, S. Light-field enhancement for the photo-catalytic applications. *physica status solidi - rapid research letters* **4**, 268 – 270 (2010).
16. Kowalska, E., Janczarek, M., Rosa, L., Juodkazis, S. & Ohtani, B. Mono- and bi-metallic plasmonic photocatalysts for degradation of organic compounds under UV and visible light irradiation. *Catal. Today* **230**, 131–137 (2014).
17. Iwase, H., Kokubo, S., Juodkazis, S. & Misawa, H. Suppression of ripples on Ni surface via a polarization grating. *Opt. Express* **17**, 4388–4396 (2009).
18. Juodkazis, S., Mizeikis, V., Matsuo, S., Ueno, K. & Misawa, H. Three-dimensional micro- and nano-structuring of materials by tightly focused laser radiation. *Bull. Chem. Soc. Jpn.* **81**, 411–448 (2008).
19. Wang, H., Wang, K., Liu, J., Dai, H. & Yang, Z. Theoretical research on terahertz air-breakdown coherent detection with the transient photocurrent model **20**, 19264 (2012).
20. Thomson, M. D., Kress, M., Löffler, T. & Roskos, H. G. Broadband THz emission from gas plasmas induced by femtosecond optical pulses: from fundamentals to applications. *Laser Photon. Rev.* **1**, 349 – 368 (2007).
21. Johnson, P. B. & Christy, R. W. Optical constants of the noble metals. *Phys. Rev. B* **6**, 4370–4379 (1972).

## Author contributions statement

This study was primarily designed and conducted by K.H., F.C.P.M., and W.H.H, as the principal investigators, provided conceptual and technical guidance in all aspects of the research project. K.H. and F.C.P.M. planned and performed the X-ray intensity and X-ray emission spectra measurements. M.P., M.T.N., and T.Y. contributed the preparation and characterization of gold nano-colloidal solutions. A.B. and S.J. performed and analyzed the calculated absorption/extinction measurements and FDTD simulations. The manuscript was written by K.H. and commented on by all authors.

## Additional Information

The authors declare no competing financial interests.

## Acknowledgements

S.J. is grateful for partial support via the Australian Research Council DP130101205 Discovery project. FDTD simulation work was performed on the swinSTAR supercomputer at Swinburne University of Technology.